Progress In Electromagnetics Research C, Vol. 172, 468–479, 2026

PIER C

(Received 27 May 2026, Accepted 9 July 2026, Scheduled 23 August 2026)

A Medium to High-Speed Sensorless Control Strategy for SRMs Based on Dual-Stage Resonant Filter and Feedforward Phase-Locked Loop

Zheng Zhang[1], Zebin Yang[1,*], Xiaodong Sun[1], and Chao Sun[2]

[1]School of Electrical and Information Engineering, Jiangsu University, Zhenjiang 212013, China
[2]Automotive Engineering Research Institute, Jiangsu University, Zhenjiang 212013, China

ABSTRACT: To reduce the cost and improve the accuracy of position estimation for switched reluctance motors (SRMs) at medium-to-high speeds, this study proposes a sensorless control strategy based on a dual-stage resonant filter (DSRF) and a feedforward phase-locked loop (FPLL). First, to address issues of weak dc-offset suppression and high-frequency harmonics in the second-order generalized integrator (SOGI) when processing nonlinear flux linkage, a DSRF with ideal band-pass characteristics is proposed. This filter effectively suppresses the dc-offset and higher-order harmonics. Second, the proposed FPLL introduces a feedforward compensation path related to the speed derivative. By adding zeros to broaden the system bandwidth, the dynamic response is accelerated. The tracking accuracy and response speed of the position observer are also enhanced under variable-speed and sudden-load conditions. Finally, the effectiveness of the proposed strategy was verified on a six-phase 12/10 SRM experimental platform. The experimental results show that the proposed sensorless control strategy achieves a fast and highly accurate estimation of the rotor position and speed at medium-to-high speeds, particularly during dynamic processes, thereby enhancing system reliability and dynamic performance.

1. INTRODUCTION

Owing to its significant advantages, including a simple and rugged structure, low cost, wide speed regulation range, strong fault tolerance, and excellent robustness under harsh operating conditions such as high speed and high temperature, switched reluctance motor (SRM) has become an important research focus in fields such as electric vehicle powertrains, aerospace actuators, high-performance industrial speed control, and high-reliability household appliances, demonstrating broad application prospects [1–4]. SRM operation relies heavily on the accurate estimation of rotor position. However, the traditional sensor-based position estimation approach directly increases a system's cost, volume, and complexity. Furthermore, the sensors themselves and their associated circuitry are susceptible to degradation in environments with strong vibrations, high temperatures, dust, or corrosion, which compromises system reliability [5–7].

Therefore, research on reliable position sensorless control strategies has become increasingly important. This technology aims to calculate the rotor position and speed by detecting and processing measurable electrical signals from the motor itself, in conjunction with the motor's mathematical model or intelligent algorithms. Existing methods can be broadly classified into two categories based on the applicable speed range: low-speed and medium-to-high speed methods [8, 9].

The pulse injection method is currently one of the most widely adopted position sensorless control techniques for low-speed operation [10, 11]. This method injects high-frequency voltage pulses into the non-conducting phase windings and utilizes the periodic variation of magnetic reluctance with rotor position in SRMs. In [12], based on the current response obtained via pulse injection, a triple current-slope-difference (CSD) threshold method was proposed. This approach replaces the instantaneous value comparison with slope fitting and introduces a third threshold to indicate the zero-current position. Ref. [13] further proposed a dual-inductance dynamic threshold and position-indexed pulse-fusion strategy, which enables adaptive commutation-angle adjustment through dynamic thresholds. In addition to pulse injection method, inductance detection is another important method for SRMs [14, 15]. This method estimates rotor position by detecting the inductance of the motor winding, because an SRM's phase inductance is a single-valued function of rotor position and phase current. Inductance detection methods can be categorized into current-gradient methods [16] and incremental-inductance methods [17].

During medium-to-high-speed operation, flux-linkage characteristics are commonly used to estimate rotor position and speed. By processing the nonlinear flux linkage, signals containing position and speed information are obtained for the estimation [18–20]. In [21], an adaptive band-pass filter was used to remove dc offset and harmonics from a single-phase signal, extracting a quadrature signal related to rotor position,

* Corresponding author: Zebin Yang (zbyang@ujs.edu.cn).

while Fourier analysis was applied to compensate for the phase shifts caused by commutation. Alternatively, a dual-loop position observer extends the discrete characteristic-position estimation to a continuous linearized position function by incorporating a position adaptive law and a dual-loop structure [22]. The look-up table (LUT) approach [23–25] enables direct position estimation using flux-linkage parameters, but requires a substantial amount of offline measured data. In contrast, methods based on characteristic positions extract key feature points from current or inductance waveforms to directly estimate the rotor position, thereby eliminating the error drift associated with integration operations. Ref. [26] proposed a demagnetization inductance slope negative-going zero-crossing detection (D-ISNZ) as the main estimation algorithm, which avoids false detections caused by magnetic saturation in the excitation region and current ripple. A single-inductance threshold (SIT) remedial strategy was also designed. In [27], a combined characteristic-position detection method was presented, integrating D-ISNZ detection with back-EMF zero-crossing detection. In [28], a flux linkage interpolation model (FLIM) was constructed that only requires flux-linkage data at the aligned and unaligned characteristic positions, thereby greatly simplifying the modeling process. An adaptive gradient optimization method is further developed to perform online real-time correction of the model for accurate rotor position estimation. Ref. [29] presents a position-sensorless control strategy based on an improved sliding-mode speed controller (SMSC) and a sliding-mode position observer (SMPO) to enhance the motor's dynamic speed response and improve estimation accuracy. In [30], a novel machine-learning-based super-twisting sliding-mode observer (STSMO) was proposed, which incorporated a torque-difference estimator to enhance robustness. Furthermore, artificial intelligence methods are increasingly applied to high-speed operations. Ref. [31] proposes an optimized neural network approach for position/speed-sensorless control of SRM drives and introduces advanced angle control (AAC) to regulate the SRM speed. In [9], the modeling performance of a back-propagation neural network (BPNN) optimized via the Levenberg-Marquardt algorithm is compared with that of a radial basis function neural network (RBFNN). Another method employs an online-trained BP neural network for rotor position identification, which dynamically extracts training samples and performs the network's batch training. However, this approach requires considerable computational overhead and tends to degrade the estimation accuracy [32].

This study proposes a medium-to-high-speed sensorless control strategy for SRMs. The method estimates rotor position and speed by using the nonlinear flux-linkage characteristics. First, a novel DSRF filter is designed to overcome shortcomings of the traditional SOGI in processing nonlinear flux linkage, effectively suppressing dc offset and higher-order harmonics and extracting a clean fundamental-wave position signal. Compared with existing SOGI filters, which primarily rely on adjusting internal gains to balance dynamic response and noise suppression, the proposed DSRF constructs an ideal frequency characteristic by altering the basic topology and incorporating auxiliary high- or low-pass poles. This structural innovation effectively overcomes the inherent trade-off between suppressing integrator drift and maintaining dynamic performance in conventional designs. Second, an FPLL position observer was constructed. By introducing a feedforward term related to the speed derivative, the system bandwidth is broadened, significantly improving the dynamic tracking accuracy and response speed under variable-speed and sudden-load conditions.

2. MATHEMATICAL MODEL AND NONLINEAR MAGNETIC FLUX LINKAGE

2.1. Mathematical Model of SRMs

According to Kirchhoff's law, the basic voltage equation for an SRM's kth phase is generally expressed as follows:

$$u_k = Ri_k + \frac{d\psi(\theta_k, i_k)}{dt} \tag{1}$$

where u_k denotes the stator voltage; i_k represents the stator current; R is the stator resistance; and $\psi(\theta_k, i_k)$ is the flux linkage, which is a function of the rotor position θ_k and current i_k. θ_k specifically refers to the mechanical rotor position, expressed in electrical degrees throughout this paper.

Based on the basic voltage equation of the switched reluctance motor, the expression for the actual flux linkage can be written as:

$$\psi(\theta_k, i_k) = \begin{cases} \int (u_k - Ri_k)dt, & \theta \in [\theta_{\text{on}}, \theta_{\text{off}}] \\ 0, & \theta \in \text{others} \end{cases} \tag{2}$$

where θ_{on} and θ_{off} are turn-on and turn-off angles, respectively. Due to frequent switching of the magnetic flux path in SRMs, magnetic flux linkage is inherently discontinuous, and when the motor phase is within the turn-off angle interval, the flux is typically considered zero.

2.2. Nonlinear Magnetic Flux Linkage Model

The nonlinear flux linkage of SRMs contains information regarding the rotor position. However, the nonlinear relationship between the flux linkage, rotor position, and current makes it challenging to estimate the rotor position. To better represent this nonlinear characteristic, the flux linkage is generally expressed as a Fourier series:

$$\psi(\theta_k, i_k) = a_0 - a_1 \cos(N_r\theta) - \sum_{k=2}^{N} a_k \cos(kN_r\theta) \tag{3}$$

where a_0 represents the dc component in the Fourier series; a_1 and a_k are Fourier coefficients; N_r represents the number of rotor poles; and N represents the Fourier series.

Considering the influence of harmonics and the computational complexity of the nonlinear flux linkage, the N value is typically set to 4. Expanding (3) into a fourth-order Fourier series:

$$\begin{aligned}\psi(\theta_k, i_k) &= a_0 - a_1 \cos(N_r\theta) - a_2 \cos(2N_r\theta) \\ &\quad - a_3 \cos(3N_r\theta) - a_4 \cos(4N_r\theta)\end{aligned} \tag{4}$$

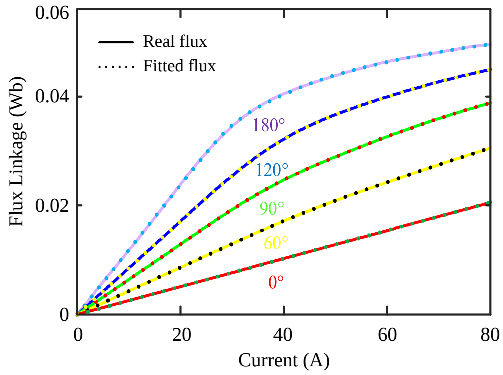

FIGURE 1. 12/10 SRM flux linkage at different rotor positions.

For a given current level, if the flux linkage values at five known rotor positions are known, the coefficients in Equation (4) can be determined by substituting positions and flux linkage values. When the positions 0°, 60°, 90°, 120°, and 180° are selected, the fitting curve is shown in Fig. 1. The expressions for the flux linkage coefficients are as follows:

$$\begin{pmatrix} 1 & 1 & 1 & 1 & 1 \\ 1 & 0.5 & -0.5 & -1 & -0.5 \\ 1 & 0 & -1 & 0 & 1 \\ 1 & -0.5 & -0.5 & 1 & -0.5 \\ 1 & -1 & 1 & -1 & 1 \end{pmatrix} \begin{pmatrix} a_0 \\ a_1 \\ a_2 \\ a_3 \\ a_4 \end{pmatrix} = \begin{pmatrix} \psi(0°) \\ \psi(60°) \\ \psi(90°) \\ \psi(120°) \\ \psi(180°) \end{pmatrix} \tag{5}$$

The flux linkage coefficients can thus be calculated as:

$$\begin{pmatrix} a_0 \\ a_1 \\ a_2 \\ a_3 \\ a_4 \end{pmatrix} = \begin{pmatrix} 1/6 & 1/3 & 0 & 1/3 & 1/6 \\ 1/3 & 1/3 & 0 & -1/3 & -1/3 \\ 1/4 & 0 & -1/2 & 0 & 1/4 \\ 1/6 & -1/3 & 0 & 1/3 & -1/6 \\ 1/12 & -1/3 & 1/2 & -1/3 & 1/12 \end{pmatrix} \begin{pmatrix} \psi(0°) \\ \psi(60°) \\ \psi(90°) \\ \psi(120°) \\ \psi(180°) \end{pmatrix} \tag{6}$$

Owing to the nonlinearity of the flux linkage, rotor position estimation based on flux linkage is highly challenging, particularly when the flux linkage is not stored in advance.

It can be seen from (4) that after the dc component and higher-order harmonics are filtered out, the remaining fundamental flux linkage expression contains the rotor position information, which is expressed as:

$$\psi_f = -a_1 \cos(N_r\theta) \tag{7}$$

where a_1 represents the amplitude of the fundamental flux linkage ψ_m. Because the flux linkage varies with the current, its value is unknown. To eliminate a_1, a sinusoidal function orthogonal ψ_{qf} is introduced and expressed as:

$$\psi_{qf} = -a_1 \sin(N_r\theta) \tag{8}$$

Based on (5) and (6), the fundamental flux linkage amplitude can be expressed as:

$$a_1 = \psi_m = \sqrt{\psi_f^2 + \psi_{qf}^2} \tag{9}$$

Based on the signal processing method described above, the fundamental flux linkage can be calculated. By removing the nonlinear components from the flux linkage, a signal that contains only position information is obtained, enabling a sensorless control strategy independent of the magnetic characteristic parameters.

2.3. The Topology of AHB Converter

The core power circuit of the switched reluctance motor is controlled using an asymmetric half-bridge (AHB) converter. Its key advantages are a completely independent control of each phase winding and strong fault-tolerance capability. Topology of the AHB converter is shown in Fig. 2. Each phase winding in the AHB converter can operate in three modes: magnetization, freewheeling, and demagnetization.

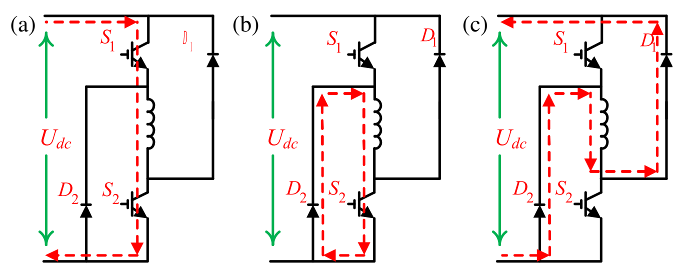

FIGURE 2. Three modes of the AHB converter. (a) The magnetization mode, (b) the freewheeling mode, and (c) the demagnetization mode.

When both S_1 and S_2 are turned on, the dc power source supplies the winding via switching devices, causing the winding current to rise rapidly, which corresponds to the magnetization mode. In the freewheeling mode, S_1 is turned off, whereas S_2 remains on. The winding current forms a closed loop through S_2 and freewheeling diode D_2, during which the current decays slowly. When both S_1 and S_1 are turned off, the energy stored in the winding is fed back to the dc power source via D_1 and D_2, resulting in a rapid decrease in current. This is referred to as the demagnetization mode. In the AHB converter, the SRM's switching states are designated as "1", "0", and "−1", corresponding to these three modes, respectively. The output signal S_k can be expressed as:

$$S_k = \begin{cases} 1\,(\text{demagnetization}) \\ 0\,(\text{freewheeling}) \\ -1\,(\text{magnetization}) \end{cases} \tag{10}$$

3. PROPOSED POSITION SENSORLESS CONTROL SCHEME

3.1. Design of the Proposed DSRF

In SRM's sensorless control, the accuracy and stability of fundamental component extraction directly determine system control precision. The conventional Second-Order Generalized Integrator (SOGI) is widely used for fundamental extraction due to its excellent quadrature output capability. When the nonlinear flux linkage signal is input, the SOGI can extract two orthogonal fundamental-wave components, whose transfer functions are expressed as:

$$G_{\text{SOGI}}(s) = \frac{k_0\omega_e s}{s^2 + k_0\omega_e s + \omega_e^2} \tag{11}$$

where k_0 represents the gain parameter of the SOGI; ω_e is the resonant frequency; and s represents the Laplace operator.

Although the SOGI offers effective fundamental-wave extraction, simple structure, and ease of engineering implementation, its practical application is constrained by certain limitations due to its single-resonant topology and the absence of auxiliary filtering. Specifically, the lack of a dedicated dc suppression stage makes it susceptible to dc offset during flux-linkage integration, leading to output drift under low-frequency operating conditions, whereas the absence of a high-frequency noise-suppression mechanism further restricts its performance. To address these issues, this study proposes a DSRF. By optimizing frequency domain characteristics and incorporating supplementary filtering stages, the proposed scheme achieves enhanced anti-interference capability and steady-state performance.

Building on the conventional SOGI, the DSRF's core design retains the SOGI's resonant fundamental extraction characteristics while integrating filtering capabilities to optimize the transfer function. This integrated approach eliminates the need for separate additional filtering stages, thereby enhancing anti-interference capability and compensating for the performance shortcomings of the conventional SOGI. DSRF's control block diagram is illustrated in Fig. 3. By inputting the nonlinear flux linkage, the required quadrature signals ψ_f and ψ_{qf} are obtained. The DSRF's open-loop transfer function is expressed as:

$$G_\psi(s) = \frac{\omega_1\omega_e^2 s^4}{(s+\omega_2)(s+\omega_1)(s^2+\omega_e^2)(s+k)} \tag{12}$$

where ω_1 and ω_2 are filter cutoff frequencies, and $\omega_1 < \omega_e < \omega_2$. The high-pass cut-off frequency is set to $\omega_1 = 0.1\omega_e$ to effectively suppress dc offsets while preserving the fundamental component, which aligns with the inherent drift characteristics of flux integration. The low-pass cut-off frequency is fixed at ten times the inverter switching frequency. The stabilization coefficient k is specified as $0.5\omega_e$.

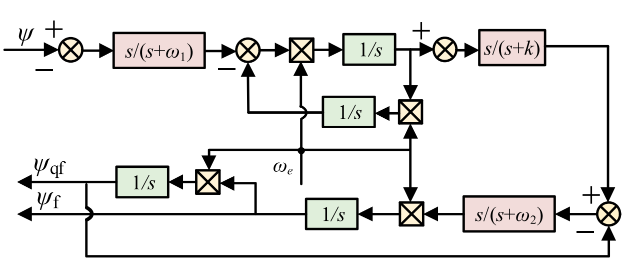

FIGURE 3. Block diagram of the proposed DSRF.

Thus, transfer functions for output quadrature signals can be expressed as:

$$G_{\psi_f}(s) = \frac{\omega_1\omega_e^2 s^3}{(s+\omega_2)(s+\omega_1)(s^2+\omega_e^2)(s+k)+\omega_1\omega_e^2 s^4} \tag{13}$$

$$G_{\psi_{qf}}(s) = \frac{\omega_1\omega_e^3 s^2}{(s+\omega_2)(s+\omega_1)(s^2+\omega_e^2)(s+k)+\omega_1\omega_e^2 s^4} \tag{14}$$

To rigorously establish the DSRF's theoretical foundation, the pole-zero placement strategy and stability analysis are conducted. The denominator of the transfer functions is a fifth-order polynomial $D(s)$:

$$D(s) = (s+\omega_2)(s+\omega_1)(s^2+\omega_e^2)(s+k)+\omega_1\omega_e^2 s^4 \tag{15}$$

The system's poles consist of a pair of conjugate poles located at $\pm j\omega_e$ to ensure frequency selectivity, and three real poles at $-\omega_1$, $-\omega_2$, and $-k$ to ensure frequency selectivity. Based on the Routh-Hurwitz criterion, since all coefficients of $D(s)$ are positive real numbers, no poles reside in the right-half plane. The stability is further guaranteed by poles' negative real parts. The coefficient k acts as a damping factor; as k increases, the dominant poles move further left from the imaginary axis, enhancing the system's disturbance-rejection capability.

The Bode diagram performance of the proposed DSRF is shown in Fig. 4. From the perspective of magnitude-frequency characteristics, the conventional SOGI relies solely on a single resonant pole for fundamental component extraction. In the low-frequency range, it provides almost no suppression of dc offset and low-frequency integration drift. In the high-frequency range, its attenuation slope is merely -20 dB/dec, which fails to effectively attenuate inverter switching noise and high-order harmonics, leading to significant offset in the output signal. In contrast, the DSRF incorporates both high-pass and

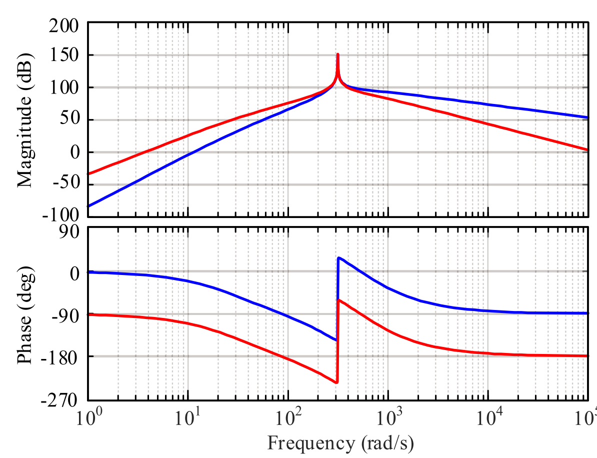

FIGURE 4. Bode diagram of the proposed DSRF.

low-pass poles into its transfer function, forming ideal band-pass characteristics of strong low-frequency attenuation, a flat mid-frequency passband, and rapid high-frequency roll-off. In the low-frequency range, the gain rapidly approaches negative infinity, which can completely block the dc components and low-frequency drift, fundamentally eliminating cumulative error from flux-linkage integration. In the mid-frequency range, the gain remained close to unity, allowing the fundamental signal to pass without distortion and maintaining excellent fundamental extraction capability. In the high-frequency range, the attenuation slope increased to -40 dB/dec, providing stronger suppression of high-frequency harmonics and significantly improving the smoothness of the output waveform.

In terms of phase-frequency characteristics, the DSRF optimizes the pole placement, resulting in a noticeably reduced phase lag at the fundamental frequency. The phase response across the entire band-pass exhibits gentle variation and good linearity. The quadrature output maintained a high-precision 90° phase difference with strong amplitude consistency. Even under operating conditions with speed fluctuations, the phase error remains within a very small range, demonstrating excellent dynamic robustness.

3.2. The Proposed Position Observer

The conventional phase-locked loop (PLL) performs well in tracking rotor position under constant-speed conditions, and the transfer function of the PLL error is expressed as:

$$G_{\varepsilon\text{-PLL}}(s) = \frac{-s^2}{s^2 + k_p s + k_i} \tag{16}$$

where k_p is the proportional gain of the PLL, and k_i is the integral gain. The transfer function of a PLL is typically expressed as:

$$G_{\text{PLL}}(s) = \frac{k_p s + k_i}{s^2 + k_p s + k_i} \tag{17}$$

Conventional PLLs, such as sliding-mode observer [29], rely solely on feedback error correction. Owing to inherent stability constraints, this architecture limits the achievable bandwidth and results in a finite steady-state error when tracking ramp inputs. To address these limitations, the FPLL proposed in this paper incorporates a feedforward compensation path related to the speed derivative. Theoretically, introducing the feedforward term adds two adjustable zeros to the closed-loop transfer function. These zeros effectively counteract the phase lag caused by the poles, thereby broadening the system bandwidth without compromising stability margins. The block diagram of the proposed FPLL is shown in Fig. 5.

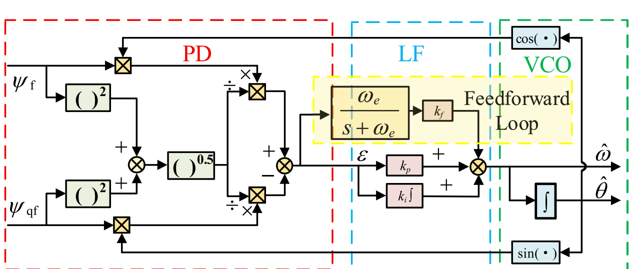

FIGURE 5. Block diagram of proposed FPLL.

The FPLL structure adds a speed-related feedforward term to the traditional PLL, thereby enhancing its dynamic tracking capability. The closed-loop transfer function of the designed FPLL is derived as follows:

$$G_{\text{FPLL}}(s) = \frac{s^2(k_f\omega_c + k_p) + s(k_p\omega_c + k_i) + k_i\omega_c}{s^3 + s^2(k_p + \omega_c) + s(k_p\omega_c + k_i) + k_i\omega_c} \tag{18}$$

where k_f denotes the feedforward gain. The feedforward path directly introduces a speed derivative-related term that compensates for the dynamic phase lag in advance, thereby enhancing the structure of the conventional PLL.

Therefore, the FPLL's characteristic equation is given by:

$$s^3 + s^2(k_p + \omega_e) + s(k_p\omega_e + k_i) + k_i\omega_e = 0 \tag{19}$$

Since all coefficients are positive real numbers, the necessary condition for stability is satisfied according to the Routh-Hurwitz criterion. With the introduction of the feedforward gain k_f, the dominant poles shift leftward, moving farther away from the imaginary axis. This implies an increased damping ratio and an accelerated response speed. Moreover, across the entire parameter tuning range, all poles reside strictly in the left-half plane, demonstrating that the FPLL has inherently stronger stability than the conventional PLL.

The error transfer function is then modified as follows:

$$G_{\varepsilon\_\text{FPLL}}(s) = \frac{s^3 + s^2\omega_e(1-k_f)}{s^3 + s^2(k_p + \omega_e) + s(k_p\omega_e + k_i) + k_i\omega_e} \tag{20}$$

A conventional PLL exhibits a sluggish dynamic response and significant tracking errors under sudden speed variations. In contrast, the FPLL employs feedforward compensation to preemptively counteract the dynamic phase lag. By introducing a zero to broaden the system bandwidth, the FPLL achieves a markedly faster dynamic response, thereby reducing tracking errors. When the motor accelerates or decelerates, the reference speed signal can be approximated as a ramp signal r/s^2, and the input reference signal in the frequency domain for the position is then expressed as r/s^3. According to the final value theorem of the Laplace transform, the steady-state position error of the conventional PLL can be derived as:

$$\lim_{t\to\infty} \varepsilon_{\text{PLL}} = \lim_{s\to\infty} s \cdot \frac{r}{s^3} \cdot \frac{s^2}{s^2 + k_p s + k_i} = \frac{r}{k_i} \tag{21}$$

It can be seen that the PLL exhibits a fixed steady-state error in response to the ramp input signal, which persists throughout the motor acceleration process and limits the accuracy of the position estimation. In contrast, the steady-state error of the FPLL is expressed as:

$$\begin{aligned} &\lim_{t\to\infty} \varepsilon_{\text{FPLL}} \\ &= \lim_{s\to\infty} s \cdot \frac{r}{s^3} \cdot \frac{s^3 + s^2\omega_e(1-k_f)}{s^3 + s^2(k_p+\omega_e) + s(k_p\omega_e + k_i) + k_i\omega_e} \\ &= \frac{r(1-k_f)}{k_i} \end{aligned} \tag{22}$$

As shown in Equation (22), when $k_f = 1$, the steady-state error becomes zero. Unlike a standard second-order PLL, the FPLL exhibits zero steady-state error under ramp velocity inputs. By compensating for rotor displacement during acceleration, this approach markedly improves dynamic response and disturbance rejection capability. The feedforward gain k_f is selected within the validated effective range of $0.8 \leq k_f \leq 1.0$. In the experiments, k_f is set to 0.9 to strike an optimal balance between bandwidth extension and preservation of adequate phase margin. While theoretical analysis indicates that $k_f = 1.0$ yields zero steady-state error under ramp inputs, $k_f = 0.9$ is more congruent with the stringent stability requirements typical of industrial applications.

The conventional PLL is a second-order system with no closed-loop zeros, and its dynamic response is solely determined by pole locations. Due to stability consideration, the poles cannot be placed too close to the imaginary axis, which limits the system bandwidth and imposes an upper bound on response speed, making it difficult to achieve fast tracking. In contrast, the FPLL is a third-order system that introduces two closed-loop zeros, whose positions are determined by feedforward gain k_f. Introducing these zeros effectively counteracts the phase lag caused by some poles, thereby broadening the system bandwidth.

According to the FPLL's closed-loop transfer function, the expression for its zeros can be obtained as follows:

$$z_{1,2} = \frac{-(k_p\omega_e + k_i) \pm \sqrt{(k_p\omega_e + k_i)^2 - 4(k_f\omega_e + k_p)k_i\omega_e}}{2(k_f\omega_e + k_p)} \tag{23}$$

The maximum overshoot M_p and rise time t_r are given by:

$$\begin{cases} M_p \approx e^{-\pi\zeta/\sqrt{1-\zeta^2}} \cdot \left(1 + \frac{\omega_p}{|z|}\right) \\ t_r = \frac{1.8}{\zeta\omega_p} \cdot \left(1 - \frac{\zeta\omega_p}{|z|}\right) \end{cases} \tag{24}$$

where the damping ratio ζ and resonant frequency ω_p are given by:

$$\begin{cases} \zeta = \frac{k_p\omega_e + k_i}{\sqrt{2k_i\omega_e(k_p+\omega_e)}} \\ \omega_p = \sqrt{\frac{k_i\omega_e}{k_p+\omega_e}} \end{cases} \tag{25}$$

Attributing to the zeros introduced via the feedforward path, the FPLL exhibits a pronounced elevation in magnitude response that effectively neutralizes the attenuation induced by system poles. Consequently, the effective bandwidth is extended, empowering the FPLL to track rapid speed variations with high fidelity. As observed from (23) and (24), increasing the feedforward gain k_f shifts zeros closer to the imaginary axis, thereby intensifying the pole-zero cancellation effect and broadening system bandwidth. Crucially, despite this bandwidth expansion, the phase margin remains well-preserved, guaranteeing robust stability. This theoretical bandwidth advantage manifests a significantly faster tracking response for the FPLL during acceleration transients than the conventional PLL.

Based on the analysis above, to address the issues of sluggish dynamic response, large tracking errors, and slow convergence of the conventional PLL under sudden speed changes, the proposed FPLL incorporates feedforward compensation to preemptively counteract dynamic phase lag. By introducing zeros to extend the system bandwidth, the FPLL significantly improves the dynamic response speed, thereby effectively enhancing the steady-state performance of the sensorless control strategy.

TABLE 1. Comparison of the algorithmic complexity of SOGI-PLL and DSRF-FPLL.

Method	Multiplication count/period	Execution time (µs)	Memory usage (RAM)
DSRF-FPLL	8	7.6	32
SOGI-PLL	15	16.3	50

As illustrated in Table 1, the sampling frequency was set to 10 kHz on a DSP28377D experimental platform, serving as the basis for a quantitative analysis of the algorithmic complexity of the conventional SOGI-PLL and proposed DSRF-FPLL. The conventional SOGI-PLL requires 15 multiplication operations per cycle, involving integrator updates and phase-locked loop regulation, with an execution time of approximately 16.3 µs and a memory footprint of 50 bytes of RAM. In contrast, the proposed DSRF-FPLL performs 8 multiplication operations per cycle, primarily for dual-stage resonant filtering and feedforward compensation within the unified structure. It occupies 32 bytes of RAM and achieves an execution time of approximately 7.6 µs. By structurally integrating filtering and observation functions, the proposed method reduces the execution time by 8.7 µs per cycle and saves 18 bytes of memory allocation compared to the conventional approach. This streamlined computational profile, characterized by fewer arithmetic operations and lower latency, represents a highly optimized solution well-suited for resource-constrained embedded systems.

4. EXPERIMENTAL VERIFICATION

To verify the proposed sensorless control strategy, experiments were conducted on a six-phase 12/10 SRM. As shown in Fig. 6, an experimental platform was developed and includes the SRM, torque sensors, magnetic powder brake, power converter, power supply unit, and DSP control board. SRM's main parameters are listed in Table 2. The experimental results are

TABLE 2. Key parameters and dimensions of the SRM.

Parameter	SRM
Number of phases	6
Number of stator/rotor poles	12/10
Rated voltage (V)	110
Rated Torque (N·m)	8
Stator diameter (mm)	130
Air gap length (mm)	0.4
Number of turns in each pole	15

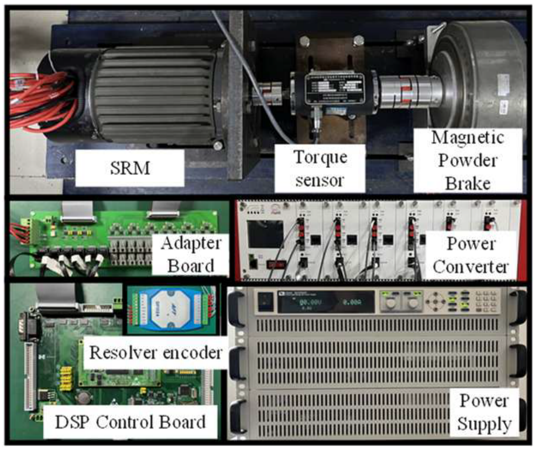

FIGURE 6. Six-phase 12/10 SRM experimental setup.

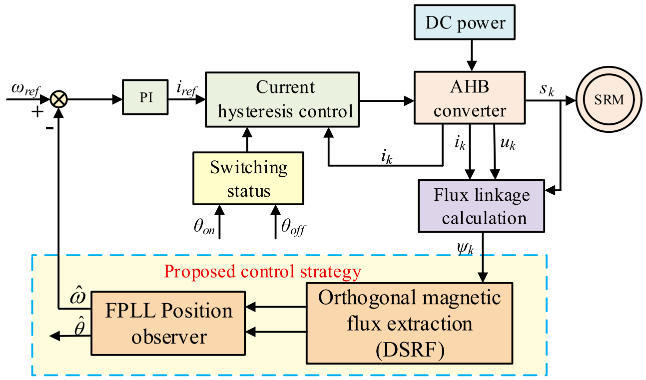

FIGURE 7. Architecture of the proposed sensorless control strategy.

displayed on an oscilloscope for an intuitive presentation. The actual rotor position was measured using six Hall position sensors. In addition, the currents of the six phases were individually monitored using six dedicated current sensors.

Figure 7 illustrates the hierarchical control structure of the proposed sensorless scheme, which includes a hysteresis current control loop and a position regulation loop. The outer speed regulation loop processes the speed error using a proportional-integral (PI) controller to generate torque and produce a reference current, ensuring stable speed tracking performance. Meanwhile, the inner current control adopts hysteresis current control, where the inverter state is rapidly switched when the current error exceeds a predefined threshold, forcing the actual motor current to closely follow the reference value. This control structure ensures robust current regulation and a dynamic speed response. The phase flux linkage obtained from phase currents and voltages measured via the power converter served as the input signal for the orthogonal signal extraction. Using the proposed DSRF, the acquired nonlinear phase flux linkage is processed to output a set of orthogonal signals containing the position information. The orthogonal flux linkage signals were then transformed by the FPLL to resolve the estimated position, thereby completing the sensorless estimation process.

To verify the accuracy of the proposed sensorless control strategy, Fig. 8 presents experimental results at 3000 r/min and 3 N·m. In Fig. 8(a), it can be observed that during the current conduction stage, the flux linkage increases approximately linearly with the rise of current, and the waveform shows no abnormal oscillation; during the current turn-off stage, the flux linkage decays rapidly to near zero, with an amplitude of approximately 0.025 Wb. Meanwhile, the current waveform also exhibits the characteristic of alternating turn-on and turn-off, which matches the operating state of the AHB converter, and its amplitude can reach 30 A. By using the proposed DSRF-FPLL method for position and speed estimation, the experimental results showed that the estimated rotor position closely matched the actual rotor position, with a maximum position error of approximately 0.86°, indicating that the proposed sensorless control strategy achieved good position-estimation performance with small error. The estimated speed can also rapidly track the reference speed, maintaining an estimation error within 5 r/min. Further experiments were conducted at 4500 r/min, and the results are shown in Fig. 9. At this speed, the rotor position estimation error remained within a small range, and the estimated speed agreed well with the reference speed. The experimental results demonstrate that the proposed control strategy maintains a higher estimation accuracy, better dynamic response, and stronger robustness under varying speed conditions than the SOGI-PLL.

To further compare the performance of the proposed control strategy, experiments were conducted under identical test conditions using the SOGI-PLL method. The results are shown in Fig. 10. Compared with the DSRF-FPLL, while the SOGI-PLL method can also accurately estimate the rotor position, its error is relatively larger: at 3000 r/min, the maximum error is about 1.32°, and at 4500 r/min, the estimation error still reaches 1.43°. The comparison indicates that the proposed method exhibits superior estimation accuracy, faster tracking response, and better performance in the medium-to-high-speed range.

To further evaluate the performance of the proposed method under varying operating conditions, experiments were conducted with speed variations. Fig. 11 shows the experimental results when the speed increased from 3000 r/min to 4500 r/min. The results indicate that during acceleration, the current increased rapidly but returned to its normal value after a brief transient. With the SOGI-PLL method, although the rotor position can be accurately estimated, the error is relatively large, reaching a maximum of approximately 2.1°. As the speed increases, the estimated speed is expected to follow and adapt to the changes in the reference speed. However, during acceleration, the estimation error increases; when the reference speed stabilizes, the estimated speed cannot quickly follow and stabilize, and it takes approximately 8 ms to return to a stable state. In contrast, when the DSRF-FPLL method was applied, the rotor position was estimated with high precision. Even under speed variations, the maximum error was only 1.72°, which is more accurate than that of the SOGI-PLL. Meanwhile, during acceleration, the estimated speed exhibits better tracking capability: it rapidly follows speed changes and quickly stabilizes after the speed variation ends, with a maximum error of only 13 r/min at the completion of the speed transition. The experimental results demonstrate that the proposed control strategy maintains a higher estimation accuracy, better dynamic

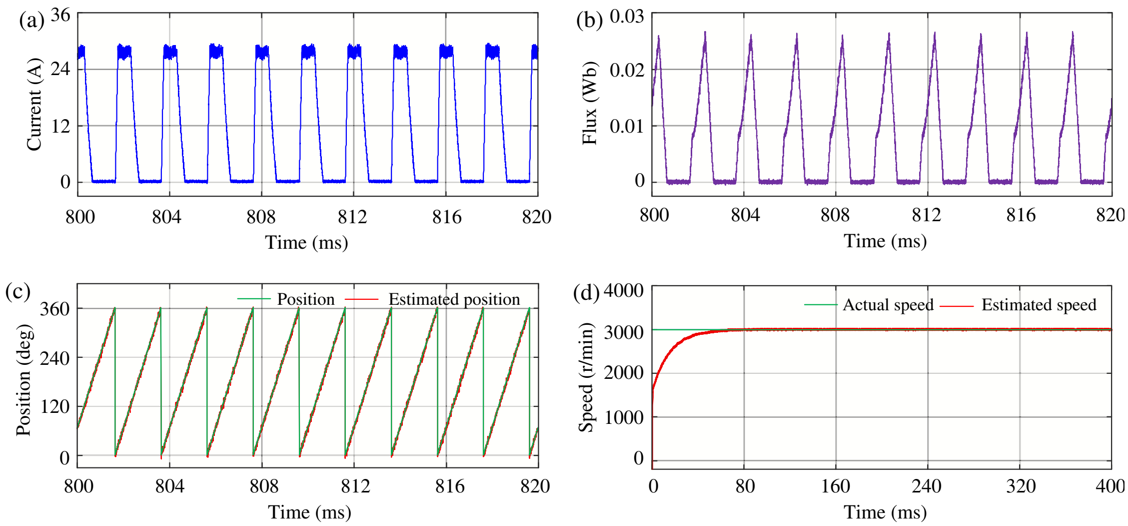

FIGURE 8. Experimental results of DSRF-FPLL at 3000 r/min. (a) Current of phase A, (b) flux linkage of phase A, (c) estimated position of phase A, and (d) estimated speed of phase A.

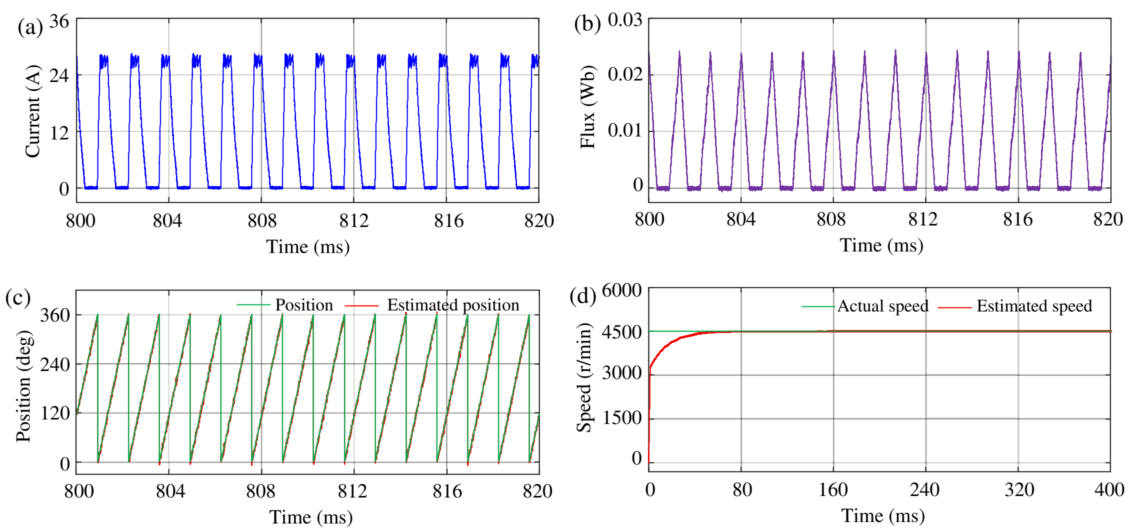

FIGURE 9. Experimental results of DSRF-FPLL at 4500 r/min. (a) Current of phase A, (b) flux linkage of phase A, (c) estimated position of phase A, and (d) estimated speed of phase A.

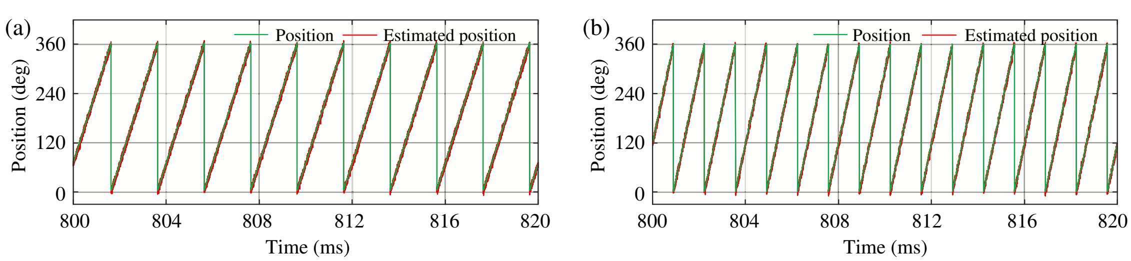

FIGURE 10. Experimental results of SOGI-PLL. (a) Results at 3000 r/min and (b) results at 4500 r/min.

response, and stronger robustness under varying speed conditions.

Results of the experiment conducted under varying load conditions are shown in Fig. 12. The motor was initially set to a load of 3 N·m, and after operating for a period, the load was increased to 4 N·m. The current varied with the load change: the phase current also changed as the load increased, with its peak rising rapidly to approximately 34 A. When the load was reduced to 3 N·m, the phase current returned to its initial value. The flux linkage exhibited a similar trend under varying loads, reaching 0.028 Wb at 4 N·m. Experimental results show that under varying loads, the SOGI-PLL method can estimate a position close to the actual position, but the maximum estimation error reaches approximately 2.5°. Moreover, the esti-

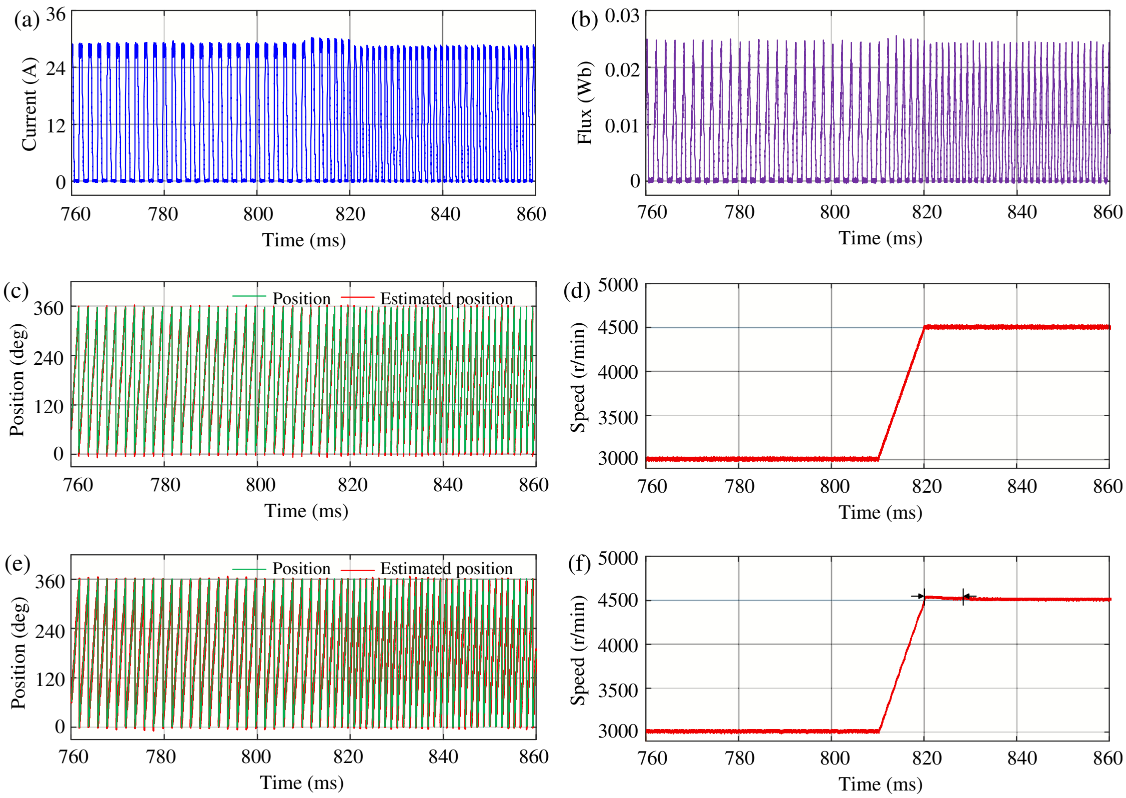

FIGURE 11. Experimental results when the speed changed from 3000 r/min to 4500 r/min. (a) Current of phase A, (b) flux linkage of phase A, (c) estimated position of DSRF-FPLL, (d) estimated speed of DSRF-FPLL, (e) estimated position of SOGI-PLL, and (f) estimated speed of SOGI-PLL.

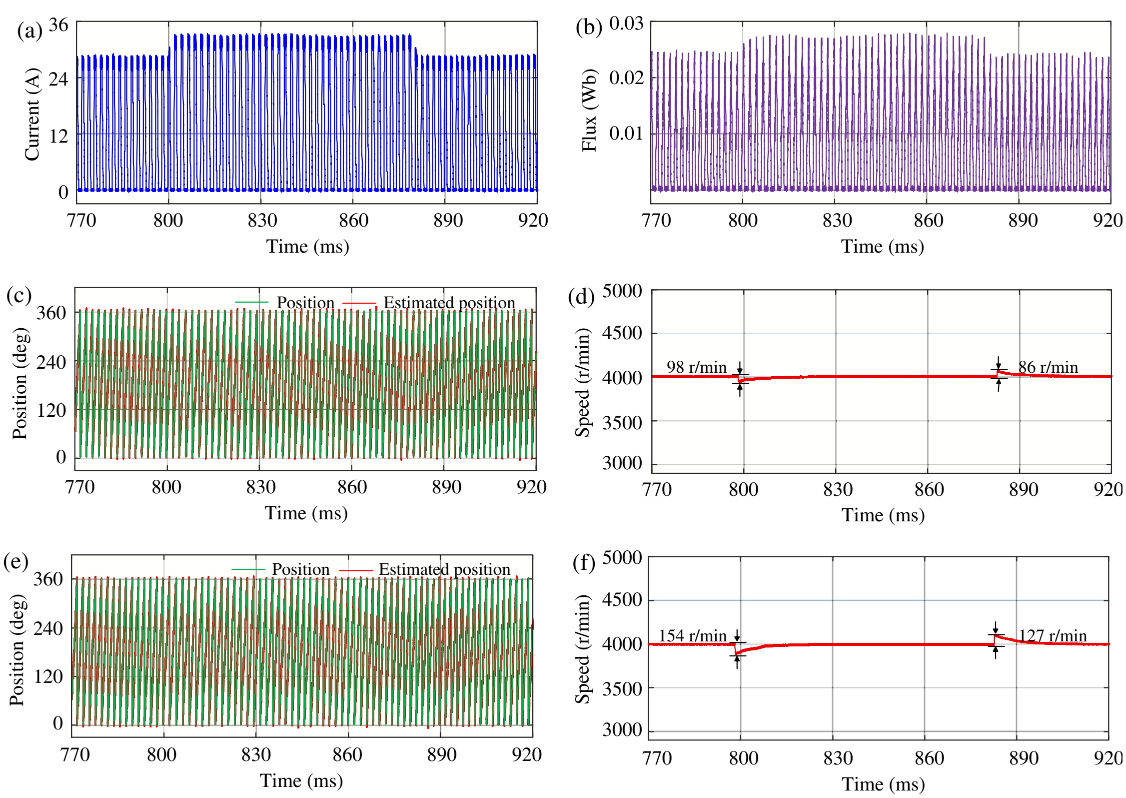

FIGURE 12. Experimental results when the load changed from 3 N·m to 4 N·m. (a) Current of phase A, (b) flux linkage of phase A, (c) estimated position of DSRF-FPLL, (d) estimated speed of DSRF-FPLL, (e) estimated position of SOGI-PLL, and (f) estimated speed of SOGI-PLL.

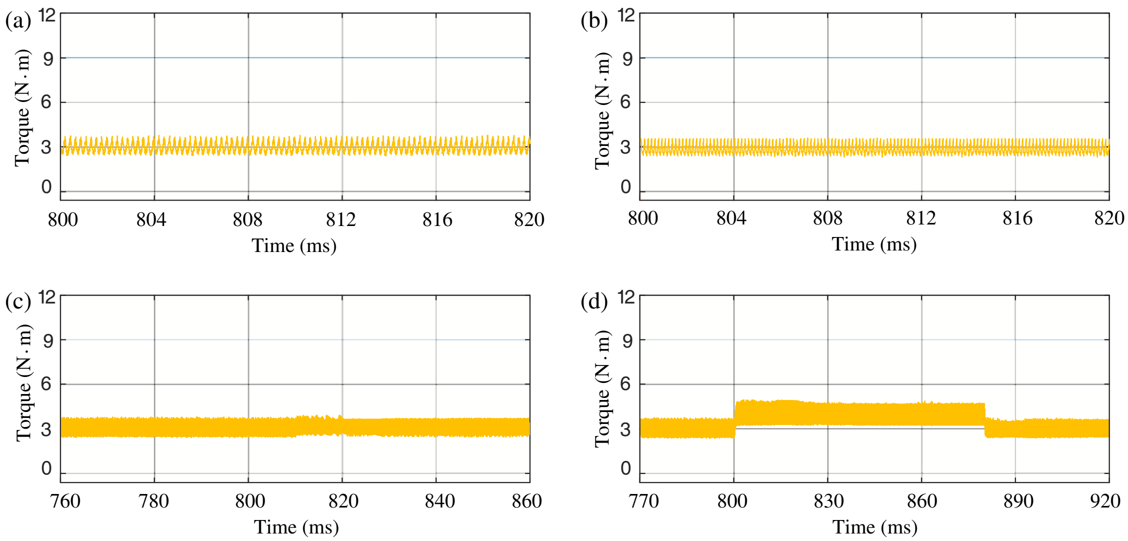

FIGURE 13. Experimental results of torque. (a) At 3000 r/min and 3 N·m, (b) at 4500 r/min and 3 N·m, (c) from 3000 r/min to 4500 r/min at 3 N·m, and (d) at 3000 r/min from 3 N·m to 4 N·m.

TABLE 3. Method performance comparison table.

Experimental conditions	Methods	Maximum position error (°)	speed error (r/min)
3000 r/min	SOGI-PLL	1.32	8
3 N·m	DSRF-FPLL	0.86	5
4500 r/min	SOGI-PLL	1.42	9
3 N·m	DSRF-FPLL	0.92	5
3000–4500 r/min	SOGI-PLL	2.1	29
3 N·m	DSRF-FPLL	1.72	13
3000 r/min	SOGI-PLL	2.5	40
3–4 N·m	DSRF-FPLL	2	16

mated speed exhibits significant fluctuations: it rapidly drops by 154 r/min at the moment of load increase, then gradually returns to the reference speed, when the load decreases and sharply rises by 127 r/min before gradually approaching the reference speed. Although the estimated speed followed the same trend as the actual speed, the speed was notably affected by load changes, resulting in a relatively large estimation error. In contrast, under the DSRF-FPLL control, the rotor position estimation error was only approximately 2°, demonstrating better accuracy. Its advantage is even more pronounced in speed estimation: during load increase, the speed drops by only 98 r/min, and during load recovery, it increases by only 86 r/min. More importantly, in terms of dynamic response, the speed variation time was significantly shorter, allowing the system to return to a steady state more quickly, indicating a superior dynamic response capability.

Figure 13 illustrates torque variations under diverse operating conditions. With operation under steady loads, torque fluctuates within a confined range, maintaining overall stability. As depicted in Fig. 13(c), during speed transients, the torque exhibits more pronounced oscillations coincident with acceleration phase. However, once the speed regulation is complete and the system returns to steady state, the torque promptly stabilizes within its nominal range. Furthermore, under abrupt load step changes, the torque dynamically adjusts in accordance with varying load demand. Nevertheless, it retains its capacity to remain stable within the expected dynamic envelope, following the cessation of the load transient.

Performance indicators are compared between the two methods, as shown in Table 3. In summary, the proposed sensorless estimation strategy not only maintains small position and speed estimation errors under fixed operating conditions, but also exhibits good robustness, high accuracy, and excellent dynamic response under varying operating conditions, making it more suitable for position and speed estimation in the medium-to-high-speed range.

5. CONCLUSION

This paper proposes a sensorless control strategy for SRMs operating in the medium-to-high-speed range, aiming to eliminate the dependence on mechanical position sensors and improve estimation accuracy. By processing the flux linkage signal with the DSRF, dc offsets and high-frequency harmonics are effectively suppressed. Furthermore, the FPLL broadens the system bandwidth by introducing a speed-differentiation term, enhancing dynamic tracking capability. Experimental results under tested conditions demonstrate that the proposed strategy achieves a maximum position error of 0.86° at 3000 r/min. Compared with the conventional SOGI-PLL, the proposed method exhibits smaller position errors and better dynamic responses during acceleration and sudden load changes. These results confirm the effectiveness of the proposed scheme in enhancing the reliability and dynamic performance of SRM drives within its specified operational range.

ACKNOWLEDGEMENT

This work was supported by the Postgraduate Research & Practice Innovation Program of Jiangsu Province under Project 26CXJH7293.

REFERENCES

[1] Sun, X., Y. Zhu, Y. Cai, M. Yao, Y. Sun, and G. Lei, "Optimized-sector-based model predictive torque control with sliding mode controller for switched reluctance motor," *IEEE Transactions on Energy Conversion*, Vol. 39, No. 1, 379–388, Mar. 2024.

[2] Chaurasiya, S. K., A. Bhattacharya, and S. Das, "Reduced switch multilevel converter for grid fed SRM drive to improve magnetization and demagnetization characteristics of an SRM," *IEEE Transactions on Industry Applications*, Vol. 59, No. 6, 6804–6816, Nov.-Dec. 2023.

[3] Sreeram, K., P. K. Preetha, J. Rodríguez-García, and C. Alvarez-Bel, "A comprehensive review of torque and speed control strategies for switched reluctance motor drives," *CES Transactions on Electrical Machines and Systems*, Vol. 9, No. 1, 46–75, Mar. 2025.

[4] Ge, L., J. Zhong, Q. Cheng, Z. Fan, S. Song, and R. W. De Doncker, "Model predictive control of switched reluctance machines for suppressing torque and source current ripples under bus voltage fluctuation," *IEEE Transactions on Industrial Electronics*, Vol. 70, No. 11, 11 013–11 021, Nov. 2023.

[5] Ge, L., H. Xu, Z. Guo, S. Song, and R. W. De Doncker, "An optimization-based initial position estimation method for switched reluctance machines," *IEEE Transactions on Power Electronics*, Vol. 36, No. 11, 13 285–13 292, Nov. 2021.

[6] Sun, X., Z. Xu, M. Pan, C. Sun, and G. Lei, "Medium-to-high speed range sensorless control of SRM drives based on unaligned rotor position estimation," *IEEE Transactions on Industrial Electronics*, Vol. 72, No. 12, 12 185–12 194, Dec. 2025.

[7] Guo, X., S. Zeng, M. Wu, R. Zhong, and W. Hua, "A direct drive sensorless starting scheme based on triple current threshold method in switched reluctance machines for low-cost current sampling applications," *IEEE Transactions on Power Electronics*, Vol. 38, No. 7, 8730–8741, Jul. 2023.

[8] Wang, H., J. Du, Z. Niu, and Y. Xue, "Estimating rotor position for SRM via regional sliding mode observer," *IEEE Transactions on Industrial Electronics*, Vol. 72, No. 1, 230–239, Jan. 2025.

[9] Cai, Y., Y. Wang, H. Xu, S. Sun, C. Wang, and L. Sun, "Research on rotor position model for switched reluctance motor using neural network," *IEEE/ASME Transactions on Mechatronics*, Vol. 23, No. 6, 2762–2773, Dec. 2018.

[10] Guo, X., S. Zeng, R. Zhong, and W. Hua, "High-precision injection current sampling scheme for direct drive low-speed position sensorless control of switched reluctance machine," *IEEE Transactions on Industrial Electronics*, Vol. 71, No. 11, 13 754–13 765, Nov. 2024.

[11] Xiao, D., J. Ye, G. Fang, Z. Xia, H. Li, X. Wang, B. Nahid-Mobarakeh, and A. Emadi, "Induced current reduction in position-sensorless SRM drives using pulse injection," *IEEE Transactions on Industrial Electronics*, Vol. 70, No. 5, 4620–4630, May 2023.

[12] Guo, X., S. Zeng, M. Wu, R. Zhong, and W. Hua, "A low-speed position sensorless scheme from standstill for low-cost SRM drives based on triple current slope difference threshold," *IEEE Transactions on Industrial Electronics*, Vol. 71, No. 4, 3296–3306, Apr. 2024.

[13] Cai, J., Y. Yan, W. Zhang, and X. Zhao, "A reliable sensorless starting scheme for SRM with lowered pulse injection current influences," *IEEE Transactions on Instrumentation and Measurement*, Vol. 70, 1–9, 2021.

[14] Ge, L., J. Zhong, C. Bao, S. Song, and R. W. De Doncker, "Continuous rotor position estimation for SRM based on transformed unsaturated inductance characteristic," *IEEE Transactions on Power Electronics*, Vol. 37, No. 1, 37–41, Jan. 2022.

[15] Sun, Q., T. Lan, X. Liu, S. Li, F. Niu, and C. Gan, "Linear inductance model reshaping-based sensorless position estimation method for SRM with antimagnetic saturation capability," *IEEE Journal of Emerging and Selected Topics in Power Electronics*, Vol. 11, No. 5, 4799–4807, Oct. 2023.

[16] Kim, J.-H. and R.-Y. Kim, "Online sensorless position estimation for switched reluctance motors using characteristics of overlap position based on inductance profile," *IET Electric Power Applications*, Vol. 13, No. 4, 456–462, Apr. 2019.

[17] Kim, J.-H. and R.-Y. Kim, "Sensorless direct torque control using the inductance inflection point for a switched reluctance motor," *IEEE Transactions on Industrial Electronics*, Vol. 65, No. 12, 9336–9345, Dec. 2018.

[18] Xiao, D., J. Ye, G. Fang, Z. Xia, and A. Emadi, "Magnetic-characteristic-free high-speed position-sensorless control of switched reluctance motor drives with quadrature flux estimators," *IEEE Journal of Emerging and Selected Topics in Power Electronics*, Vol. 10, No. 1, 220–235, Feb. 2022.

[19] Chen, Z., H. Jing, X. Wang, D. Luo, X. Wang, G. Fang, H. Zhao, and D. Xiao, "Selective harmonic elimination and dynamic enhancement in magnetic-characteristic-free sensorless control of SRM drives at high speeds," *IEEE Transactions on Power Electronics*, Vol. 39, No. 5, 5339–5348, May 2024.

[20] Wang, T., W. Ding, Y. Hu, S. Yang, and S. Li, "Sensorless control of switched reluctance motor drive using an improved simplified flux linkage model method," in *2018 IEEE Applied Power Electronics Conference and Exposition (APEC)*, 2992–2998, San Antonio, TX, USA, 2018.

[21] Chen, Z., H. Jing, X. Wang, X. Wang, G. Fang, H. Zhao, and D. Xiao, "General-purpose high-speed position-sensorless control of switched reluctance motors using single-phase adaptive observer," *IEEE Transactions on Transportation Electrification*, Vol. 10, No. 3, 5241–5249, Sep. 2024.

[22] Shao, Y., Y. Yu, and F. Chai, "Dual closed-loop position observer with nonlinearity-decoupled model for feature-flux-based sensorless SRM drives," *IEEE Transactions on Industrial Electronics*, Vol. 71, No. 1, 160–170, Jan. 2024.

[23] Ye, J., B. Bilgin, and A. Emadi, "Elimination of mutual flux effect on rotor position estimation of switched reluctance motor drives," *IEEE Transactions on Power Electronics*, Vol. 30, No. 3, 1499–1512, Mar. 2015.

[24] Gan, C., Y. Chen, Q. Sun, J. Si, J. Wu, and Y. Hu, "A position sensorless torque control strategy for switched reluctance machines with fewer current sensors," *IEEE/ASME Transactions on Mechatronics*, Vol. 26, No. 2, 1118–1128, Apr. 2021.

[25] Ralev, I., A. Klein-Hessling, B. Pariti, and R. W. De Doncker, "Adopting a SOGI filter for flux-linkage based rotor position sensing of switched reluctance machines," in *2017 IEEE International Electric Machines and Drives Conference (IEMDC)*, 1–7, Miami, FL, USA, May 2017.

[26] Zhou, D., H. Chen, X. Wang, V. F. Pires, and J. Martins, "Synthetic sensorless control scheme for full-speed range of switched reluctance machine drives with fault-tolerant capability," *IEEE Transactions on Transportation Electrification*, Vol. 8, No. 4, 4456–4469, Dec. 2022.

[27] Cai, J. and Z. Deng, "A joint feature position detection-based sensorless position estimation scheme for switched reluctance motors," *IEEE Transactions on Industrial Electronics*, Vol. 64, No. 6, 4352–4360, Jun. 2017.

[28] Yang, Y., X. Sun, Y. Wen, Z. Xu, R. Wang, A. Dianov, G. Demidova, and V. Prakht, "Sensorless control for switched reluctance motor based on adaptive gradient scheme using flux linkage interpolation model," *IEEE Transactions on Industrial Electronics*, Vol. 73, No. 3, 3792–3802, Mar. 2026.

[29] Sun, X., N. Wang, M. Yao, and G. Lei, "Position sensorless control of SRMs based on improved sliding mode speed controller and position observer," *IEEE Transactions on Industrial Electronics*, Vol. 72, No. 1, 100–110, Jan. 2025.

[30] Zhao, Y., J. Zhu, P. Ren, H. Cao, and S. Zhang, "Position-sensorless control of SRM drives based on a novel super-twisting sliding mode observer with the machine learning model," *IEEE Journal of Emerging and Selected Topics in Power Electronics*, Vol. 13, No. 5, 6178–6189, Oct. 2025.

[31] Yalavarthi, A. and B. Singh, "Sensorless speed control of SRM drive using optimized neural network model for rotor position estimation," *IEEE Transactions on Energy Conversion*, Vol. 39, No. 4, 2158–2168, Dec. 2024.

[32] Shen, X., X. Dou, S. Liu, C. Chen, X. Jiang, and W. Sun, "Simulation research on no position control strategy of switched reluctance motor based on on-line training of BP neural network," in *2023 International Seminar on Computer Science and Engineering Technology (SCSET)*, 644–647, New York, NY, USA, 2023.